

Design and calibration of a high-sensitivity and high-accuracy polarimeter based on liquid crystal variable retarders

Jing Guo^{1,2}, De-Qing Ren^{1,2,3}, Cheng-Chao Liu^{1,2}, Yong-Tian Zhu^{1,2}, Jiang-Pei Dou^{1,2}, Xi Zhang^{1,2} and Christian Beck⁴

¹ National Astronomical Observatories/Nanjing Institute of Astronomical Optics & Technology, Chinese Academy of Sciences, Nanjing 210042, China; jguo@niaot.ac.cn

² Key Laboratory of Astronomical Optics & Technology, Nanjing Institute of Astronomical Optics & Technology, Chinese Academy of Sciences, Nanjing 210042, China

³ Physics and Astronomy Department, California State University Northridge, 18111 Nordhoff Street, Northridge, California 91330-8268, USA

⁴ National Solar Observatory, Boulder, CO 80303, USA

Received 2016 August 12; accepted 2016 October 13

Abstract Polarimetry plays an important role in the measurement of solar magnetic fields. We developed a high-sensitivity and high-accuracy polarimeter (HHP) based on nematic liquid crystal variable retarders (LCVRs), which has a compact setup and no mechanical moving parts. The system design and calibration methods are discussed in detail. The azimuth error of the transmission axis of the polarizer as well as the fast axes of the two LCVRs and the quarter-wave plate were determined using dedicated procedures. Linearly and circularly polarized light were employed to evaluate the performance of the HHP. The experimental results indicate that a polarimetric sensitivity of better than 5.7×10^{-3} can be achieved by using a single short-exposure image, while an accuracy on the order of 10^{-5} can be reached by using a large number of short-exposure images. This makes the HHP a high-performance system that can be used with a ground-based solar telescope for high-precision solar magnetic field investigations.

Key words: instrumentation: polarimeters — methods: laboratory — Sun: magnetic fields — techniques: polarimetric

1 INTRODUCTION

It is well-known that activity on the Sun is dominated by its magnetic fields. As such, polarized radiation from the Sun contains a wealth of information on its magnetic fields, and solar polarimetry provides us with a great opportunity to research and interpret solar phenomena related to the spatial structure of local solar magnetic fields, such as solar wind, radio wave flux, solar flares, coronal mass ejections, coronal heating and sunspots (del Toro Iniesta 2003). The aim of solar polarimetry is to determine the full Stokes parameters of incident light, and usually, together with a spectrograph, information about solar magnetic fields can be obtained through the Zeeman or Hanle effects (Stenflo 2013). As early as 1908, Hale used a Fresnel rhomb and a rotatable Nicol

prism (i.e., polarimetry) to photographically detect the Zeeman splitting of spectral lines observed in sunspots and to validate the presence of strong magnetic fields in sunspots (Hale 1908). From that beginning, polarimetry has played an important role in solar observations, and a polarimeter is considered to be an inherent part of solar instrumentation (Elmore 2011).

The 1-meter New Vacuum Solar Telescope (NVST) is China's new-generation large high-technology solar facility (Liu & Xu 2011; Wang et al. 2013). Its scientific goals include observing the Sun with very high spatial and spectral resolution in the wavelength range from 0.3 to 2.5 μm , detecting small-scale structures and fine details in the evolution of solar magnetic fields, and studying other key questions related to solar activities (Liu 2014). Currently, the polarimeter NVST em-

employs a rotating modulation system with classical wave plates (Liu et al. 2014). This kind of traditional polarization modulator has also been used by many other solar polarimeters, e.g., the Advanced Stokes Polarimeter (ASP; Skumanich et al. 1997), the Diffraction-Limited Spectro-Polarimeter (DLSP; Sankarasubramanian et al. 2003), the Polarimetric Littrow Spectrograph (POLIS; Beck et al. 2005), the Spectro-Polarimeter for Infrared and Optical Regions (SPINOR; Socas-Navarro et al. 2006), etc. However, the utilization of rotating parts can lead to instrument jitter that decreases measurement accuracy and increases the mass and volume of the system as well (Iglesias et al. 2016). These disadvantages are more serious for space-borne instruments, for which resources are very limited and which have the risk of mechanical failure (Alvarez-Herrero et al. 2011).

Fortunately, with the development of liquid crystals (LCs), liquid crystal variable retarders (LCVRs), which function as variable wave plates, are an attractive alternative to traditional rotary polarizing optics, since the polarization state of a light beam can be actively controlled by varying the voltage applied to the LCVR without any mechanical movements (Shih et al. 2014; Zangrilli et al. 2003). The absence of moving parts can provide quick switching times on the order of a few milliseconds. Together with short exposure times, this makes it possible to freeze atmospheric turbulence with a ground-based telescope. Furthermore, LCVRs have a broad wavelength range in the visible with low optical losses. As a consequence, polarization modulation by LCVRs is very promising, and several LCVR-based solar polarimeters have been developed in recent years, e.g., the Facility InfraRed Spectropolarimeter (FIRS) installed at the Dunn Solar Telescope (DST) (Jaeggli et al. 2010), the KIS/IAA Visible Imaging Polarimeter (VIP) operated at the German Vacuum Tower Telescope (Beck et al. 2010) and the Imaging Magnetograph eXperiment (IMaX) on board the Sunrise balloon-borne solar observatory (Martínez Pillet et al. 2011). This type of polarimeter is able to reach a high polarimetric sensitivity on the order of 10^{-3} .

In this paper, we describe the development and testing of a high-sensitivity and high-accuracy polarimeter (HHP), which consists of a pair of temperature-stabilized nematic LCVRs, a Wollaston prism (WP) and a charge-coupled device (CCD) camera. The HHP is superior to the above LCVR-based polarimeters in terms of polarimetric accuracy and system speed. Section 2 provides a detailed description of the system design and associated algorithms developed to achieve the design goal. Section 3 gives our calibration procedures for the polarization el-

ements. Section 4 describes polarimetric results and how the polarimetric sensitivity and accuracy were evaluated. Section 5 presents the discussion. Finally, we give our conclusions in Section 6.

2 THEORY

For ground-based solar polarimetry, one should particularly pay attention to atmospheric seeing, since it will introduce spurious polarization signals. With most of the seeing power contained in the 1-100 Hz frequency range (Judge et al. 2004), a modulation frequency of the order of 100 Hz is required to reliably reconstruct the four polarization components I , Q , U and V (Krishnappa & Feller 2012). Consequently, seeing-induced crosstalk can be eliminated by using a very high modulation frequency in a single-beam polarimeter. For instance, the Zürich Imaging Polarimeter (ZIMPOL) employs piezo-elastic modulators with a frequency of 50 kHz, but a dedicated CCD detector must be used, in which three out of four rows of the sensor are covered and a microlens array is attached (Gandorfer et al. 2004). Although our LCVRs can finish the polarization modulation scheme within 1.2 ms (with a total of four independent retardance combinations) by using an appropriate strategy (retardance decrease takes a much shorter time than the equivalent retardance increase), the modulation frequency is mainly limited by the frame rate of the camera we currently use (109 fps), which will be updated very soon with a fast camera using a frame rate of up to 400–800 fps. Currently, our design implements a dual-beam configuration and a Wollaston prism which encodes polarization into intensity with opposite signs for the two beams. The seeing-induced crosstalk thus cancels out during the demodulation procedures.

2.1 System Design

In the laboratory, the optical setup for the light feed was composed of an He-Ne laser ($\lambda = 632.8$ nm), a collimating lens, a pinhole (PH) and a field stop (FS). A nanoparticle linear polarizer (P, extinction ratio $> 10^5 : 1$ in the range 600–1200 nm) plus a quarter-wave plate (QWP, @632.8 nm) acted as a polarization state generator (PSG), which was used to generate different known polarization states that were needed to evaluate the polarimetric accuracy of the system. A pair of LCVRs was employed as the polarization modulator and a Wollaston prism as the dual-beam polarization analyzer. The fast axes of the LCVR1 and LCVR2 were mounted at 0° and 45° , respectively, and one transmission axis of the Wollaston prism was oriented at 0° . The LCVRs (man-

ufactured by Thorlabs) are AR coated for visible light from 350–700 nm. They can generate a wide retardance range from 30 nm to λ . The LC controller LCC25 provides active DC offset compensation while applying an AC voltage. It is worth noting that the properties of the LC materials are temperature-dependent, and the generated retardance will deviate from its desired value owing to the temperature variation (Herederer et al. 2007). Therefore, each LCVR is equipped with a temperature sensor and heater, which will hold the temperature of the retarder constant to within $\pm 0.1^\circ\text{C}$ when used with a TC200 temperature controller. The temperature stabilization provides constant retardance even if the ambient temperature changes and also allows for faster switching times. The Wollaston prism (manufactured by Altechna) is made of quartz (extinction ratio $> 2 \times 10^3 : 1$ in the range 200–2300 nm) with an angular field of $1^\circ @ 632.8 \text{ nm}$. A non-polarizing beamsplitter (BS) in front of the CCD camera and a high accuracy optical power meter (OPM, with a resolution of 1 nW) were used

in the azimuth calibrations of the polarization elements (see Sect. 3). The CCD (manufactured by Imperx, model: B0610, readout noise: 16 electrons) is a 16-bit camera with 640×480 pixels and a pixel size of $7.4 \mu\text{m} \times 7.4 \mu\text{m}$. In the experiments, the LCVRs and the CCD camera were controlled by LabVIEW, and working temperatures of the LCVRs were set to 30.0°C . The optical layout of the HHP is shown in Figure 1.

2.2 Modulation and Demodulation Algorithms

According to the HHP setup and Mueller calculus, the relationship between input and output Stokes vectors S_{in} and S_{out} is given by

$$S_{\text{out}} = M_W \cdot M_{\text{LCVR}2} \cdot M_{\text{LCVR}1} \cdot S_{\text{in}}, \quad (1)$$

where M_{LCVR} and M_W are Mueller matrices of the LCVR and the Wollaston prism, respectively, which can be expressed by

$$M_{\text{LCVR}i} = \begin{pmatrix} 1 & 0 & 0 & 0 \\ 0 & \cos^2 2\alpha_i + \sin^2 2\alpha_i \cos \delta_i & \cos 2\alpha_i \sin 2\alpha_i (1 - \cos \delta_i) & -\sin 2\alpha_i \sin \delta_i \\ 0 & \cos 2\alpha_i \sin 2\alpha_i (1 - \cos \delta_i) & \sin^2 2\alpha_i + \cos^2 2\alpha_i \cos \delta_i & \cos 2\alpha_i \sin \delta_i \\ 0 & \sin 2\alpha_i \sin \delta_i & -\cos 2\alpha_i \sin \delta_i & \cos \delta_i \end{pmatrix}, \quad (2)$$

$$M_W = \frac{1}{2} \begin{pmatrix} 1 & \cos 2\beta^\pm & \sin 2\beta^\pm & 0 \\ \cos 2\beta^\pm & \cos^2 2\beta^\pm & \cos 2\beta^\pm \sin 2\beta^\pm & 0 \\ \sin 2\beta^\pm & \cos 2\beta^\pm \sin 2\beta^\pm & \sin^2 2\beta^\pm & 0 \\ 0 & 0 & 0 & 0 \end{pmatrix}, \quad (3)$$

where α_i and δ_i denote the azimuth of the fast axis and the retardance of the i -th LCVR, respectively, β is the azimuth of the transmission axis of the Wollaston prism, and the positive and negative signs indicate two orthogonal polarized parts, respectively.

The intensity measured by the CCD camera is given by

$$L^\pm = \frac{1}{2} (I \pm \cos \delta_2 Q \pm \sin \delta_1 \sin \delta_2 U \mp \cos \delta_1 \sin \delta_2 V), \quad (4)$$

where L^+ and L^- are the intensities of the two orthogonal polarized images, respectively. In order to retrieve the four Stokes parameters in Equation (4), at least four different modulation states have to be constructed. Consequently, a modulation strategy from the IMaX is used, since it makes polarization modulation efficiencies attain their maximum values, while guaranteeing fast switching times of the LCVRs (Uribe-Patarroyo et al. 2008). The retardance combinations are as follows

$$(\delta_1, \delta_2) = (315^\circ, 305.264^\circ), (315^\circ, 54.736^\circ), (225^\circ, 125.264^\circ), (225^\circ, 234.736^\circ). \quad (5)$$

Finally, the four Stokes parameters can be computed using the observed intensities of the two orthogonally polarized images for the polarization states described above by

$$\begin{cases} I = \frac{1}{4} [(L_1^+ + L_2^+ + L_3^+ + L_4^+) + (L_1^- + L_2^- + L_3^- + L_4^-)], \\ Q = \frac{\sqrt{3}}{4} [(L_1^+ + L_2^+ - L_3^+ - L_4^+) - (L_1^- + L_2^- - L_3^- - L_4^-)], \\ U = \frac{\sqrt{3}}{4} [(L_1^+ - L_2^+ - L_3^+ + L_4^+) - (L_1^- - L_2^- - L_3^- + L_4^-)], \\ V = \frac{\sqrt{3}}{4} [(L_1^+ - L_2^+ + L_3^+ - L_4^+) - (L_1^- - L_2^- + L_3^- - L_4^-)], \end{cases} \quad (6)$$

where L_i is the measured intensity under the i -th retardance combination of the LCVRs.

3 CALIBRATIONS

Although the two LCVRs, the Wollaston prism, the polarizer and the QWP are mounted on separate rotation stages, it is essential to calibrate the azimuths of these polarization elements first. Their actual azimuths may differ from ideal values owing to the mounting errors. Any misalignment is a major factor that limits the polarimetric accuracy. To address this issue, a reference horizontal direction along the long side of the focal plane of the CCD camera is selected and all azimuths are calibrated with respect to the reference direction in the following sequence.

3.1 Azimuth of Transmission Axis of the Wollaston Prism

After the light feed optics was set up, the imaging optics and the CCD camera were installed, the Wollaston prism was mounted and the two light spots created by the Wollaston prism were adjusted to be located in the left and right half of the focal plane. Then, we could calibrate one azimuth of the transmission axes by rotating the Wollaston prism while calculating central coordinates of the two light spots. When their longitudinal coordinates are equal to each other, the orientation of the transmission axis is parallel to the reference direction, and the Wollaston prism is fixed in that orientation. A fast and effective centroid algorithm can then be employed

$$\begin{cases} x_{\text{cent}}^{\pm} = \frac{\sum_{i=1}^M \sum_{j=1}^N j L_{i,j}^{\pm}}{\sum_{i=1}^M \sum_{j=1}^N L_{i,j}^{\pm}} \\ y_{\text{cent}}^{\pm} = \frac{\sum_{i=1}^M \sum_{j=1}^N i L_{i,j}^{\pm}}{\sum_{i=1}^M \sum_{j=1}^N L_{i,j}^{\pm}} \end{cases}, \quad (7)$$

where M and N are the numbers of pixels representing the length and width of the focal plane, respectively; for the positive sign, $i = 1 \sim M/2$, and for the negative sign, $i = M/2 \sim M$.

Figure 2 illustrates the calibrated azimuth calculated using the central coordinates of the two light spots in 100 measurements. The result reveals that one azimuth of the Wollaston prism is within $1'$ with respect to the reference horizontal direction after calibration.

3.2 Azimuth of Transmission Axis of the Polarizer

The polarizer is then added into the optical path, and according to the Malus law, one of the light spots will reach minimum intensity when the azimuth of the transmission axis of the polarizer is parallel to the reference direction (perpendicular to the other transmission axis

of the Wollaston prism). In the experiments, we found that the intensity has a flat area within a small azimuth range around the crossed orientation, where all intensities are about equal to the minimum value. Therefore, the high accuracy optical power meter had to be used. We first adjusted the intensity to some specific values and recorded their azimuths, and then the parallel azimuth could be determined by calculating the mean value of the recorded azimuths. A schematic diagram of the calibration method is shown in Figure 3, while the results are listed in Table 1.

3.3 Azimuths of Fast Axes of the LCVRs and the Quarter-Wave Plate

When the retarder is placed between the polarizer and the Wollaston prism, the transmitted intensity is given by

$$L = L_0[\cos^2 \alpha - \sin 2\varphi \sin 2(\varphi - \alpha) \sin^2(\delta/2)], \quad (8)$$

where α is the relative azimuth of the transmission axis between the polarizer and the Wollaston prism, φ is the relative azimuth of the fast axis between the retarder and the transmission axis of the polarizer, and δ is the retardance. If $\alpha = 90^\circ$ and $\varphi = 0$, then the azimuth of the fast axis of the retarder is parallel to the reference direction and the transmitted intensity will reach the minimum value. The azimuths of the fast axes of the retarders are calibrated separately in a manner similar to that presented in Section 3.2. Calibrated results are shown in Table 2.

3.4 Retardances of the LCVRs

Since the LCVRs have a variable retardance, it is important to obtain the relationship between applied voltages and generated retardances. According to the setup of the HHP, a voltage-dependent transmission technique is applied, and the retardance can be calculated from the transmitted intensities ratio L_{\perp}/L_{\parallel} (Wu et al. 1984; Liu et al. 2016). The merit of this method is that the effect of intensity fluctuation in the light source can be eliminated. One LCVR is placed between the polarizer and the Wollaston prism. The transmission axis of the polarizer is at 0° and the fast axis of the LCVR is at 45° as shown in Figure 4.

The two LCVRs are calibrated individually by applying voltages from 0 to 7 V with an interval of 0.01 V, and then the retardances are interpolated with an interval of 0.001 V. The results are shown in Figure 5.

Figure 5 indicates that the relationship between applied voltages and generated retardances apparently exhibits non-linearity. The retardance stays at a constant value when the voltage is less than a threshold of about

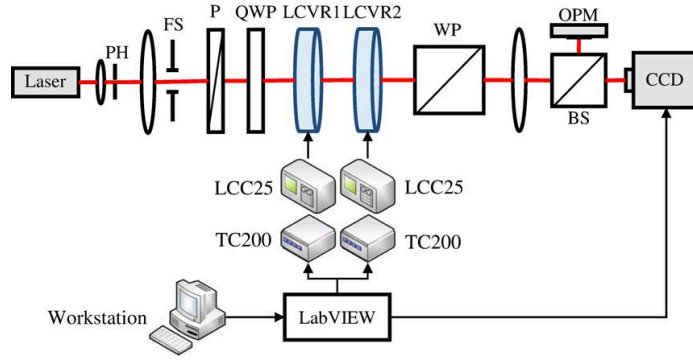


Fig. 1 Optical layout of the HHP. PH: pinhole. FS: field stop. P: polarizer. QWP: quarter-wave plate. LCVR: liquid crystal variable retarders. WP: Wollaston prism. LCC25: LC controller. TC200: temperature controller. BS: beamsplitter. OPM: optical power meter. CCD: charge-coupled device.

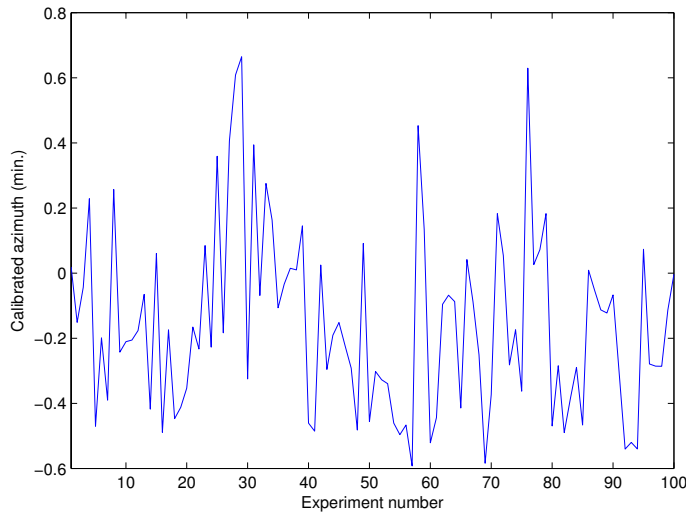


Fig. 2 Calibrated azimuth of transmission axis of the Wollaston prism with respect to the reference horizontal direction.

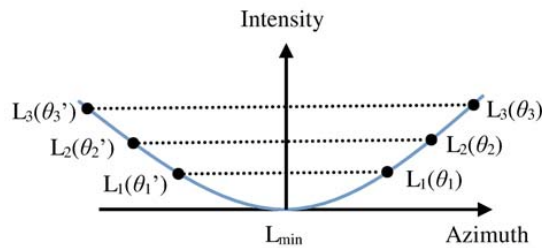


Fig. 3 Schematic diagram of the calibration method used for the transmission axis of the polarizer.

1 V. When the voltage is increased beyond this threshold, the retardance decreases dramatically in a certain voltage range at first and then gradually converges to a nonzero value. This is due to the LC molecules that are anchored at the substrate because they cannot be tilted by the electric field.

We developed an automatic calibration procedure by LabVIEW, which is convenient and fast. The calibration for each LCVR can be accomplished within 3 minutes. The four voltages of each LCVR that need to be applied to generate the desired retardances are shown in Table 3.

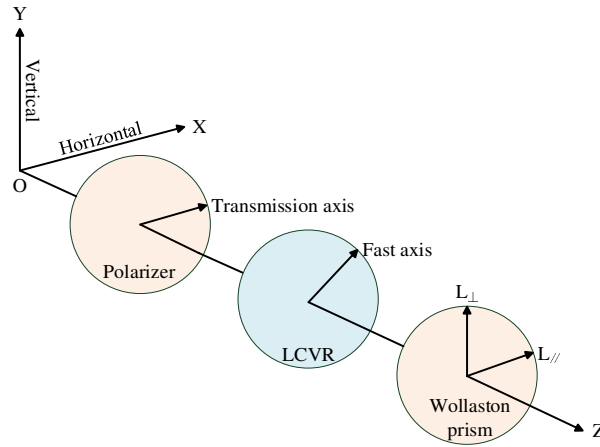


Fig. 4 Configuration of retardance calibration of the LCVR.

Table 1 Azimuth calibration of transmission axis of the polarizer

Intensity ($10^{-2} \mu\text{W}$)	Recorded azimuth	Mean value	Calibrated azimuth
4.0	$1^{\circ}30'$; $-2^{\circ}40'$	$-35'$	
5.0	$2^{\circ}30'$; $-4^{\circ}0'$	$-45'$	$-43'$
6.0	$3^{\circ}20'$; $-5^{\circ}0'$	$-50'$	

Table 2 Azimuth calibration of fast axes of the LCVRs and the QWP

Elements	Intensity ($10^{-2} \mu\text{W}$)	Recorded azimuth	Mean value	Calibrated azimuth
LCVR1	4.0	$2^{\circ}20'$; $-2^{\circ}0'$	$10'$	
	5.0	$3^{\circ}10'$; $-3^{\circ}15'$	$-3'$	$3'$
	6.0	$4^{\circ}10'$; $-4^{\circ}5'$	$3'$	
LCVR2	4.0	$0^{\circ}40'$; $-2^{\circ}10'$	$-45'$	
	5.0	$1^{\circ}50'$; $-3^{\circ}0'$	$-35'$	$38'$
	6.0	$2^{\circ}30'$; $-3^{\circ}40'$	$-35'$	
QWP	4.0	$2^{\circ}0'$; $-1^{\circ}55'$	$3'$	
	5.0	$2^{\circ}30'$; $-2^{\circ}20'$	$5'$	$4'$
	6.0	$3^{\circ}5'$; $-3^{\circ}0'$	$3'$	

4 RESULTS

In the experiments, all acquired images were first processed with dark subtraction and flat field correction. Typical results of retrieved Stokes parameters from horizontal linearly polarized light $(1, 1, 0, 0)^T$ are shown in Figure 6. According to the diameter of the light spot, we select a plot area of 25×25 pixels. Stokes Q , U and V are normalized to the intensity I .

Figure 6 reveals that the dual-beam analysis successfully retrieved the four Stokes parameters and that the intensity I shows a typical distribution of a light spot. The values of Stokes Q/I , U/I and V/I agree well with

those of horizontal linearly polarized light. We found that the retrieved results began to depart from their theoretical values when the area is larger than 18×18 pixels, since their signal-to-noise ratio is lower than $\sim 10^2$. Therefore, the performance of the HHP is evaluated using polarimetric results within this area. The polarimetric sensitivity is measured directly from one set of images that consists of four images as discussed previously according to the previous equations, which yields 4.2×10^{-3} in our measurement. The accuracy is typically quantified by the root-mean-square (RMS) noise of the Stokes parameters based on the sensitivity measurements in a large number

Table 3 Four Voltages of Each LCVR Determined after Retardance Calibration

	LCVR1				LCVR2			
Desired retardance (deg.)	315	315	225	225	305.264	54.736	125.264	234.736
Applied voltage (V)	1.164	1.164	1.578	1.578	1.280	4.617	2.480	1.614

Table 4 Polarimetric Sensitivity Evaluated by Different Polarization States

	Polarization states					
	LP0	LP45	LP90	LP135	RCP	LCP
RMS noise	3.7×10^{-3}	4.0×10^{-3}	4.1×10^{-3}	3.5×10^{-3}	5.1×10^{-3}	5.7×10^{-3}

Notes—LP: linear polarization; RCP: right circular polarization; LCP: left circular polarization.

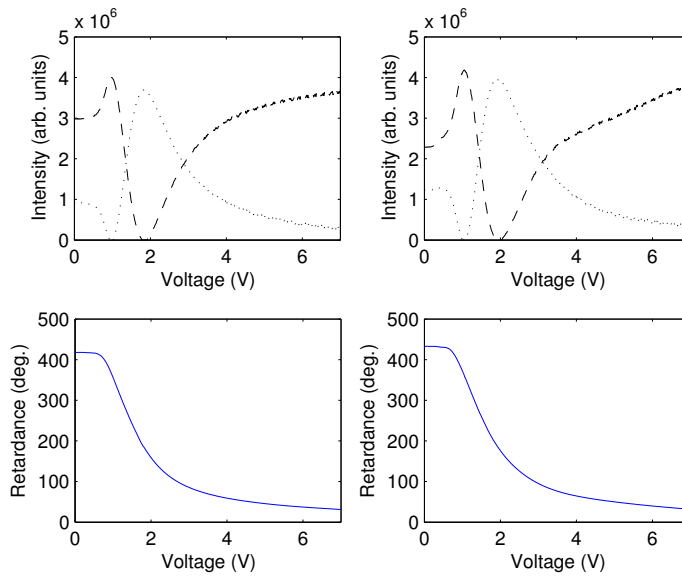


Fig. 5 Retardance calibration. *left*: LCVR1 and *right*: LCVR2. *dashed line*: L_{\perp} and *dotted line*: L_{\parallel} .

of sets of measurements (Beck et al. 2005). Since this RMS value decreases with the square root of the number of images, as shown in Figure 7, 10000 sets of images, which is a typical value for the accuracy evaluation (Povel 1995), will yield an accuracy of 4.6×10^{-5} for our polarimeter system.

Furthermore, four linearly polarized (polarizer at 0° , 45° , 90° and 135° , respectively) and two circularly (right-handed and left-handed) polarized states are generated by the PSG, and their separate RMS noises (mean value of 20 measurements per condition) are shown in Table 4.

Table 4 shows that RMS noises are better than 4.1×10^{-3} and 5.7×10^{-3} for the linearly and circularly polarized states, respectively. Because of the retardance error associated with the QWP ($< \lambda/300$ provided by the

manufacturer), polarimetric sensitivity of the circularly polarized light is a little lower than that of the linearly polarized case. From the above analyses, we can conclude that the performance of our HHP is satisfactory and stable.

5 DISCUSSION

We are scheduled to purchase a scientific CMOS camera with a high frame rate (manufactured by PCO, with 400 fps @ 2048×512 pixels and a pixel size of $6.5 \mu\text{m} \times 6.5 \mu\text{m}$) and low readout noise (1.4 electrons at highest speed), which will replace the existing Imperx B0610 camera that has a readout-noise of 16 electrons, and thus will provide a sensitivity better than 5.0×10^{-4} and an accuracy of 4.0×10^{-6} . An integral field unit (IFU) that can

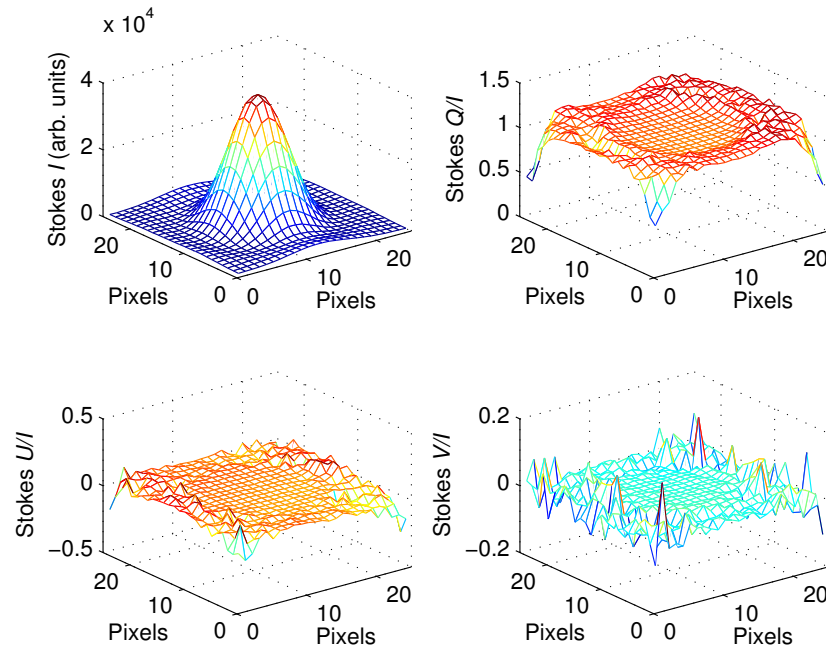


Fig. 6 Retrieved Stokes parameters from horizontal linearly polarized light.

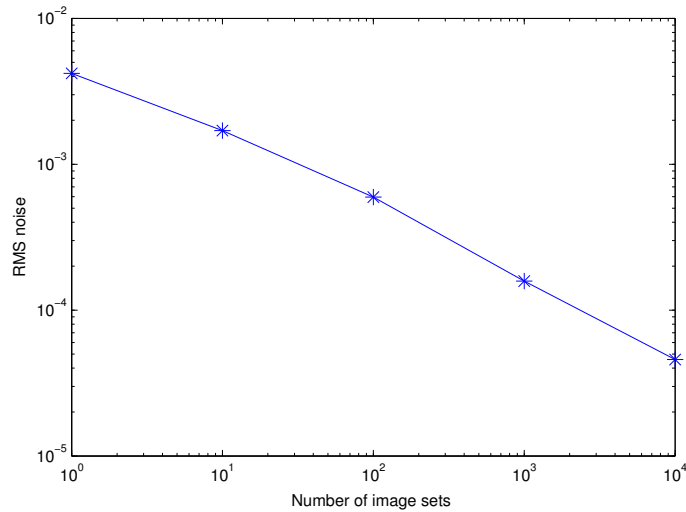


Fig. 7 Measured RMS noise tested by different sets of images.

acquire spectral information across a two-dimensional field of view (i.e. a data cube) in a single exposure is being developed by a team led by Drs. Ren and Beck for the National Solar Observatory (NSO) Horizontal Spectrograph with the DST (Beck et al. 2016, in preparation). The HHP will be used with the NSO Horizontal Spectrograph for its first test observations in 2017.

As a first step, the HHP (including several dedicated software packages) was developed and tested in the laboratory, and the performance of the HHP was evaluated as well. In the next step, the HHP will be used as instrumentation in a visit to the NSO Horizontal Spectrograph for its first test observations in 2017, and at Yunnan Observatories as part of a long-term plan. The HHP is also available to the astronomical community.

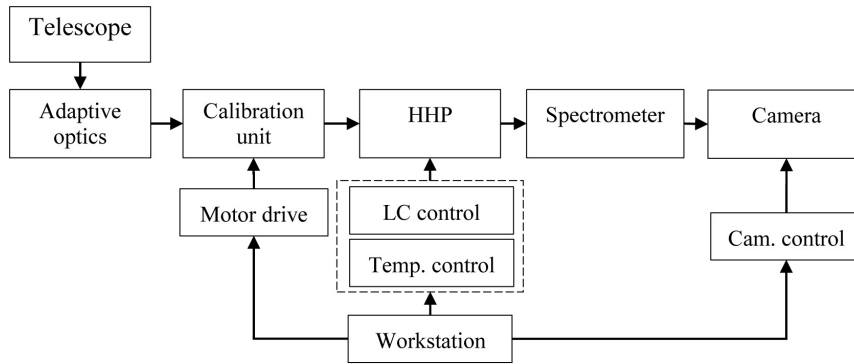


Fig. 8 The HHP interfaced with the telescope and spectrometer.

Because of its modular design, the HHP can be conveniently interfaced with a telescope and spectrometer, as shown in Figure 8.

The light coming from the telescope and the adaptive optics system firstly passes through the instrument calibration unit (ICU, which consists of a rotatable linear polarizer and a rotatable QWP and is used to derive the response function of the system). The ICU can be inserted or removed from the optical train if necessary. Then, the LCVR-based modulator of the HHP applies polarization modulation to the incident light and angle of the spectrograph grating can be determined by selecting the desired wavelength. After this, the modulated intensities are received and recorded by the CCD camera. The complete system is controlled by a workstation.

The HHP is initially used to measure the magnetic fields of the mid-photosphere using Fe I 6302 Å in the visible. In the future, the HHP will be extended to measure the magnetic fields of the photosphere using Si I 10827 Å and the high chromosphere using He I 10830 Å in the near-infrared when equipped with an infrared camera.

6 CONCLUSIONS

Developing high-performance polarimeters is a persistent goal of solar instrumentation because of their importance for measuring solar magnetic fields. We have developed and described a high-sensitivity and high-accuracy polarimeter based on LCVRs. Its performance is sufficient for use in accurate polarimetry of solar magnetic fields. We estimate that the updated HHP, with its high-sensitivity combined with the high temporal resolution of the NSO IFU spectrograph, will be a unique instrument for solar magnetic field observations. As part of a long-term plan, we will also use our HHP with the ex-

isting spectrograph at NVST for scientific investigations related to solar magnetism.

Acknowledgements This work was funded by the National Natural Science Foundation of China (NSFC, Grant Nos. 11661161011, 11433007, 11220101001, 11328302, 11373005 and 11303064), the Opening Project of Key Laboratory of Astronomical Optics & Technology, Nanjing Institute of Astronomical Optics & Technology, Chinese Academy of Sciences (CAS-KLAOT-KF201606), the “Strategic Priority Research Program” of the Chinese Academy of Sciences (Grant No. XDA04075200), the special fund for astronomy of CAS (2015–2016), the special funding for Young Researcher of Nanjing Institute of Astronomical Optics & Technology, the International Partnership Program of the Chinese Academy of Sciences (Grant No.114A32KYSB20160018), as well as the Mt. Cuba Astronomical Foundation.

References

- Alvarez-Herrero, A., Uribe-Patarroyo, N., Parejo, P. G., et al. 2011, in *SPIE Optical Engineering+ Applications*, International Society for Optics and Photonics, 8160, 81600Y
- Beck, C., Bellot Rubio, L. R., Kentischer, T. J., Tritschler, A., & Del Toro Iniesta, J. C. 2010, *A&A*, 520, A115
- Beck, C., Schmidt, W., Kentischer, T., & Elmore, D. 2005, *A&A*, 437, 1159
- del Toro Iniesta, J. C. 2003, *Introduction to Spectropolarimetry* (Cambridge: Cambridge Univ. Press)
- Elmore, D. F. 2011, in *Astronomical Society of the Pacific Conference Series*, 437, *Solar Polarization 6*, eds. J. R. Kuhn, D. M. Harrington, H. Lin, S. V. Berdyugina, J. Trujillo-Bueno, S. L. Keil, & T. Rimmele, 309

- Gandorfer, A. M., Steiner, H. P. P., Aebersold, F., et al. 2004, *A&A*, 422, 703
- Hale, G. E. 1908, *ApJ*, 28, 315
- Heredero, R. L., Uribe-Patarroyo, N., Belenguer, T., et al. 2007, *Appl. Opt.*, 46, 689
- Iglesias, F. A., Feller, A., Nagaraju, K., & Solanki, S. K. 2016, *A&A*, 590, A89
- Jaeggli, S. A., Lin, H., Mickey, D. L., et al. 2010, *Mem. Soc. Astron. Italiana*, 81, 763
- Judge, P. G., Elmore, D. F., Lites, B. W., Keller, C. U., & Rimmele, T. 2004, *Appl. Opt.*, 43, 3817
- Krishnappa, N., & Feller, A. 2012, *Appl. Opt.*, 51, 7953
- Liu, C.-C., Ren, D.-Q., Zhu, Y.-T., Dou, J.-P., & Guo, J. 2016, *RAA (Research in Astronomy and Astrophysics)*, 16, 73
- Liu, Z. 2014, in *Astronomical Society of the Pacific Conference Series*, 489, *Solar Polarization 7*, eds. K. N. Nagendra, J. O. Stenflo, Q. Qu, & M. Samoprna, 247
- Liu, Z., & Xu, J. 2011, in *Astronomical Society of India Conference Series*, 2, 9
- Liu, Z., Xu, J., Gu, B.-Z., et al. 2014, *RAA (Research in Astronomy and Astrophysics)*, 14, 705
- Martínez Pillet, V., Del Toro Iniesta, J. C., Álvarez-Herrero, A., et al. 2011, *Sol. Phys.*, 268, 57
- Povel, H.-P. 1995, *Optical Engineering*, 34
- Sankarasubramanian, K., Elmore, D. F., Lites, B. W., et al. 2003, in *Proc. SPIE*, 4843, *Polarimetry in Astronomy*, eds. S. Fineschi, 414
- Shih, W.-T., Hsieh, M.-L., & Chao, Y. F. 2014, in *SPIE Optical Engineering+ Applications*, International Society for Optics and Photonics, 920009
- Skumanich, A., Lites, B. W., Pillet, V. M., & Seagraves, P. 1997, *ApJS*, 110, 357
- Socas-Navarro, H., Elmore, D., Pietarila, A., et al. 2006, *Sol. Phys.*, 235, 55
- Stenflo, J. O. 2013, *A&A Rev.*, 21, 66
- Uribe-Patarroyo, N., Alvarez-Herrero, A., Heredero, R. L., et al. 2008, *Physica Status Solidi C Current Topics*, 5, 1041
- Wang, R., Xu, Z., Jin, Z.-Y., et al. 2013, *RAA (Research in Astronomy and Astrophysics)*, 13, 1240
- Wu, S.-T., Efron, U., & Hess, L. D. 1984, *Appl. Opt.*, 23, 3911
- Zangrilli, L., Fineschi, S., Loreggia, D., et al. 2003, *Mem. Soc. Astron. Italiana*, 74, 528